

Article

Flood Predictability of One-Way and Two-Way WRF Nesting Coupled Hydrometeorological Flow Simulations in a Transboundary Chenab River Basin, Pakistan

Ehtesham Ahmed ¹ , Naeem Saddique ^{2,3,*}, Firas Al Janabi ⁴, Klemens Barfus ², Malik Rizwan Asghar ⁵, Abid Sarwar ³  and Peter Krebs ¹

- ¹ Institute of Urban and Industrial Water Management, Technische Universität Dresden, 01069 Dresden, Germany; ehtesham.ahmed@tu-dresden.de (E.A.); peter.krebs@tu-dresden.de (P.K.)
- ² Institute of Hydrology and Meteorology, Technische Universität Dresden, 01062 Dresden, Germany; klemens.barfus@tu-dresden.de
- ³ Department of Irrigation and Drainage, University of Agriculture, Faisalabad 38000, Pakistan; abidsarwar@uaf.edu.pk
- ⁴ Global Water and Climate Adaption Centre, Technische Universität Dresden, 01062 Dresden, Germany; firas.aljanabi@tu-dresden.de
- ⁵ Flood Forecasting Division, Pakistan Meteorological Department, Islamabad 44000, Pakistan; malik.rizwan@pmd.gov.pk
- * Correspondence: naeem.saddique@tu-dresden.de

Abstract: Remote sensing precipitation or precipitation from numerical weather prediction (NWP) is considered to be the best substitute for in situ ground observations for flood simulations in transboundary, data-scarce catchments. This research was aimed to evaluate the possibility of using a combination of a satellite precipitation product and NWP precipitation for better flood forecasting in the transboundary Chenab River Basin (CRB) in Pakistan. The gauge-calibrated satellite precipitation product, i.e., Global Satellite Mapping of Precipitation (GSMaP_Gauge), was selected to calibrate the Integrated Flood Analysis System (IFAS) model for the 2016 flood event in the Chenab River at the Marala Barrage gauging site in Pakistan. Precipitation from the Global Forecast System (GFS) NWP, with nine different lead times up to 4 days, was used in the calibrated IFAS model to predict the flood hydrograph in the Chenab River. The hydrologic simulations, with global GFS forecasts, were unable to predict the flood peak for all lead times. Then, the Weather Research and Forecasting (WRF) model was used to downscale the precipitation forecasts with one-way and two-way nesting approaches. In the WRF model, the CRB was centered in two domains of 25 km and 5 km resolutions. The downscaled precipitation forecasts were subsequently supplied to the IFAS model, and the predicted simulations were compared to obtain the optimal flood peak simulation in the Chenab River. It was found in this study that the simulated hydrographs, at different lead times, from the precipitation of two-way WRF nesting exhibited superior performance with the highest R^2 and Nash–Sutcliffe efficiency (NSE) and the lowest percent bias (PBIAS) compared with one-way nesting. Moreover, it was concluded that the combination of GFS forecast and two-way WRF nesting can provide high-quality precipitation prediction to simulate flood hydrographs with a remarkable lead time of 96 h when applying coupled hydrometeorological flow simulation.

Keywords: sub-daily simulation; distributed hydrologic modelling; flood forecasting; IFAS; transboundary river; numerical weather prediction (NWP)



Citation: Ahmed, E.; Saddique, N.; Al Janabi, F.; Barfus, K.; Asghar, M.R.; Sarwar, A.; Krebs, P. Flood Predictability of One-Way and Two-Way WRF Nesting Coupled Hydrometeorological Flow Simulations in a Transboundary Chenab River Basin, Pakistan. *Remote Sens.* **2023**, *15*, 457. <https://doi.org/10.3390/rs15020457>

Academic Editors: A. K. M. Azad Hossain and Taufique Mahmood

Received: 15 December 2022

Revised: 9 January 2023

Accepted: 10 January 2023

Published: 12 January 2023



Copyright: © 2023 by the authors. Licensee MDPI, Basel, Switzerland. This article is an open access article distributed under the terms and conditions of the Creative Commons Attribution (CC BY) license (<https://creativecommons.org/licenses/by/4.0/>).

1. Introduction

Floods are one of the major causes of natural hazards due to heavy or excessive precipitation over steep terrain, saturated soil, or the poor infiltration of soil. Comprehensive knowledge of precipitation processes at higher resolutions has become important for flood forecasting and flood monitoring. Reliable and accurate precipitation data are crucial for not

only flood forecasting but also the study of climate variability and trends [1–3]. Currently, the main methods of retrieving precipitation information for flood modelling are as follows: traditional rain gauge observations, weather radar precipitation, satellite-based remote sensing precipitation, and precipitation from numerical weather prediction (NWP) [4–7].

In situ rain gauge observations are considered to be the most reliable measurements and to serve as the best input for hydrological simulations [8]. However, the acquisition of rain gauge data has various drawbacks, such as missing temporal records, poor spatial coverage, low rain gauge density, and inaccessibility in the case of transboundary catchments [9–13]. As remote sensing technologies have evolved in the last few decades, the drawbacks of temporal and spatial coverage, as well as transboundary issues, have been solved with the use of satellite precipitation products (SPPs), such as Climate Prediction Center (CPC) Morphing (CMORPH) [14], Precipitation Estimation from Remotely Sensed Information using Artificial Neural Networks (PERSIANN) [15], Tropical Rainfall Measuring Mission (TRMM) [16], Global Precipitation Measurement (GPM) [17], and Global Satellite Mapping of Precipitation (GSMaP) [18]. Nevertheless, rain gauge records and SPPs are still lagging behind in flood forecasting due to less lead time and coarser resolutions, which decrease the efficiency of flood forecasting [14,17,19].

These issues can be resolved in quantitative precipitation forecast (QPF), i.e., statistical QPF and dynamic QPF. Statistical QPF includes time-series models [20], artificial intelligence [21], and wavelet-based methods [22]. Dynamical QPF is a method of solving the equations and laws that govern the atmosphere process. The spatial distribution of precipitation and its dynamics are solved by physical governing equations in NWP models [23]. Since the description of resolved processes, the parametrization of unresolved processes, and the spatiotemporal resolution of NWP models have improved, the purpose of lead time and finer resolutions of precipitation output have nearly been achieved [24,25].

NWP models are generally divided into general models (GMs) and regional models (RMs) based on a range of simulation areas. GMs cover the global scale, while RMs cover delimited domains that are typically nested from the GMs domain. Compared with GMs, RMs give more detailed spatial distributions and more accurately capture extreme precipitation events [26]. Therefore, GMs' output can be used as input to RMs to obtain precipitation forecasts at the regional level [27]. The most commonly used RMs are: the next-generation Weather Research and Forecasting (WRF) model [28,29], the European Center for Medium-Range Weather Forecasts (ECMWF) model [30], the National Meteorological Center (NMC) forecast model [31], the operational Japan Meteorological Agency (JMA) mesoscale model [32], and the numerical forecast model of the China Meteorological Agency [33]. In this study, the WRF (version 4.0) model was implemented to enhance the resolution of the global NWP model. The downscaling of global NWP by RMs effectively improves forecasting capabilities by considering more realistic atmospheric circulations and topographies [34–37]. For instance, [38] used NWP rainfall for the rainfall–runoff–inundation of the 2010 flood in the Kabul River basin, Pakistan, and concluded that the reliability of NWP was improved after downscaling with the WRF. The authors of [39] applied WRF for the downscaling of ECMWF Re-Analysis (ERA-Interim) temperature and precipitation in Greece. Their results revealed a good correlation for seasonal patterns, and the WRF model outperformed the results of the coarse-resolution ERA-Interim.

Various methods and models that are capable of simulating floods using remotely sensed data have recently been developed. This study focused on a distributed hydrological model, i.e., the Integrated Flood Analysis System (IFAS) [40], for flood simulation in the Chenab River Basin (CRB) in Pakistan. The IFAS was developed by the International Centre for Water Hazard and Risk Management (ICHARM) in Japan and is suitable for flood prediction in large and data-scarce river basins. The IFAS model has several benefits, e.g., it is a concise tool kit with a user-friendly graphic user interface (GUI) and a straightforward parameter manager for sensitivity analysis, the visualization of flood results, and free distribution. The IFAS model can automatically collect and extract geographical, soil-type, and land-use data to set up a river basin model for flood simulations. It can utilize

both satellite and ground-based precipitation data as input. The easy incorporation of ground-based precipitation data enables the use of NWP precipitation in the IFAS model.

The IFAS is a kinematic wave approximation model used by many researchers to model floods in different areas of the world, including Pakistan [41–44]. For instance, [45] used near real-time GSMaP-NRT data for the simulation of discharge in the Chenab and Jhelum rivers in Pakistan with the IFAS and found that GSMaP-NRT products had to be corrected before hydrologic application. The authors of [46] applied gauge-adjusted GSMaP-Gauge data to the CRB in the IFAS model for calibration and used three global NWP models with a 12 h simulation interval to predict the precipitation forecast pattern in the CRB. They concluded that downscaled NWP data were more effective in flood simulations than global NWP models. Some studies have used other hydrological models in the CRB to perform flood simulations with the help of remote sensing SPPs. For example, [47] studied the CRB with the application of three SPPs, i.e., Integrated Multi-satellitE Retrievals for GPM (IMERG-F), Real Time TRMM (3B42RT), and GSMaP_NRT; they applied the Hydrologic Modeling System (HEC-HMS) model to simulate peak flow, and IMERG-F outperformed the rest of the SPPs. The authors of [48] used The Soil & Water Assessment Tool (SWAT) model for hydrological simulation in the CRB with two SPPs (IMERG-F and 3B42), and they concluded that IMERG-F outperformed the 3B42 precipitation product at daily and monthly timescales. Moreover, [49] evaluated the daily and sub-daily IMERG-E, IMERG-L, and IMERG-F products for daily and monthly flow simulations over the CRB. They concluded that the sub-daily SPPs showed superiority over the daily SPPs among all three datasets. This study was a further continuation of the abovementioned studies to improve the accuracy of flood simulation in the CRB with the application of NWP, i.e., Global Forecast System (GFS). Many studies have also been conducted with a combination of atmospheric–hydrologic models [50–53]. For instance, [52] coupled the Liuxihe model with the WRF model. They optimized the Liuxihe model parameters with rain-gauge precipitation and then re-optimized them with the WRF NWP. They concluded that the flood forecasting produced by coupling the Liuxihe model with the WRF NWP provided a good reference for a large watershed flood warning due to its long lead time. The authors of [53] also proposed the feasibility of simulating urban floods via a WRF–SWMM system, which was able to simulate the entire process from the precipitation produced by atmospheric movements to the development of urban floods. In this study, the IFAS model was coupled with WRF NWP to assess the feasibility of floods in the CRB.

Pakistan is prone to climate change and will face wetter conditions in the future, especially over the monsoon region [54], so more floods are expected. From 1950 to the end of 2020, Pakistan faced a financial loss of US\$ 38,169 million, a death toll of approximately 13,262, and 616,558 km² of area inundated by flood waters [55]. Floods become more critical to handle in the case of a transboundary river, as upstream countries do not really follow data-sharing practices [27]. Pakistan shares about 97% of the CRB (above the Marala Barrage gauging site; see Figure 1) with India, from where it is hard to obtain ground-based precipitation data due to the Jammu and Kashmir conflict [45,56]. Moreover, conventional flood forecasting using precipitation gauges and river discharge gauges cannot mitigate catastrophic damage due to small lead times. Fewer lead times will undoubtedly affect the efficiency of flood warnings and the evacuation of people on time, particularly in underdeveloped countries [57]. SPPs and NWP data are perfect alternatives to ground observations for flood forecasting in such transboundary basins [58]. The objectives of this study were identical to the described concerns, which are:

- (1) To calibrate the hydrological Integrated Flood Analysis System (IFAS) model on the transboundary Chenab River Basin (CRB) using an open-source satellite precipitation product (SPP), elevation, soil, and land use.
- (2) To apply the calibrated IFAS model for hydrometeorological flow simulations using Global Forecast System (GFS) NWP, downscaled one-way WRF, and two-way WRF GFS precipitation to obtain the optimal flood peak of the 2016 flood in the CRB.

- (3) To conduct flood forecasting with the calibrated IFAS model by using different forecast lead times of GFS precipitations.

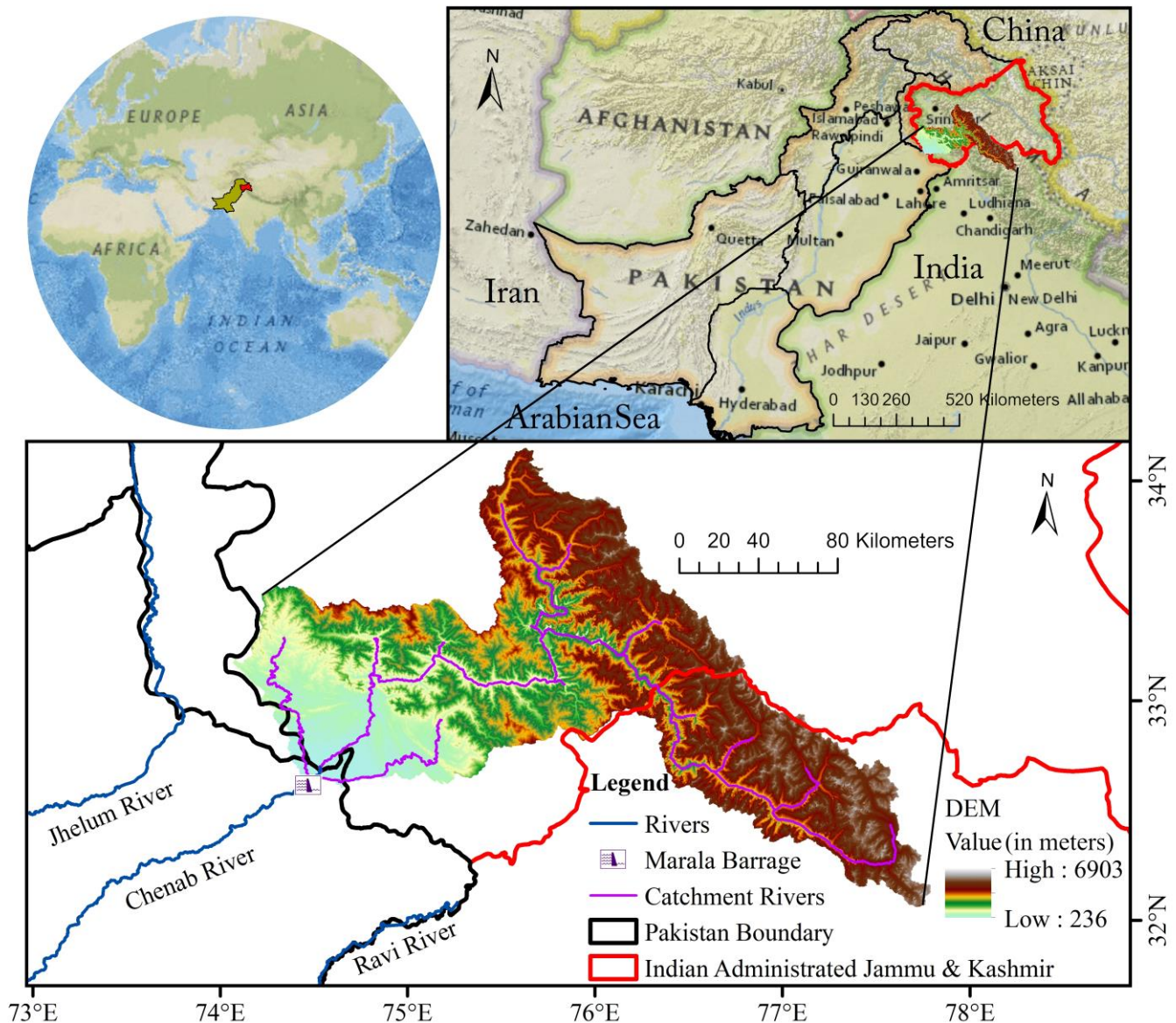


Figure 1. Study area of the Chenab River Basin.

2. Study Area

The Chenab River is one of the main eastern tributaries of the Indus River, which originates from the state of Himachal Pradesh in India and moves in the southwest direction towards Pakistan. It has a steep slope (25 m/km) in upstream snowy parts and a less steep slope (0.4 m/km) in the downstream plains of Punjab, Pakistan [59]. It has a first discharge gauging site at Marala Barrage in Pakistan. The Chenab River Basin (CRB), above the Marala Barrage, is a shared transboundary catchment between India and Pakistan, with 97% of the area on the Indian side. The elevation of the CRB ranges from 236 m to 6903 m (Figure 1). The total area of the CRB, above Marala Barrage, is about 28,000 km² and extends between 32°–34.3°N and 74°–77.85°E, as shown in Figure 1.

The CRB lies in an active monsoon belt and snow-dominant area. It receives about 65% of its precipitation in the monsoon and pre-monsoon seasons, and 26% of its precipitation is in the form of snow in winter [60]. Moreover, 84% of the river flow occurs due

to combined flow from snowmelt and rainfall in the pre-monsoon and monsoon seasons (April–September) [61].

3. Materials and Methods

3.1. Topographic, Land-Use, and Soil-Type Data in IFAS Model

In this study, the Global Map Elevation ver2 dataset was retrieved from the Global Data Archive of Geospatial Information Authority of Japan (GSI) (<https://www.gsi.go.jp/ENGLISH/> accessed on 15 September 2022), which was previously provided by the secretariat of International Steering Committee for Global Mapping (ISCGM). These data were used for a digital elevation model in the IFAS model. The Global Land Cover Characterization dataset was obtained from (<https://doi.org/10.5066/F7GB230D> accessed on 15 September 2022) and used as land-use data in the IFAS model for the CRB. The land-use classification consists of 24 categories in the CRB, which were parameterized into 5 classes in the IFAS model, as shown in Table 1. The soil-type data were obtained from the FAO-UNESCO Digital Soil Map of the World (DSMW) (<https://data.apps.fao.org/> accessed on 15 September 2022) to perform the parameterization of the aquifer tank in the CRB. Eight classes of soil were found in the CRB, i.e., Lithic, Orthic Luvisol, Glacier, Haplic Phaeozem, Chromic Luvisol, Eutric Fluvisol, Gleyic Cambisol, and Eutric Gleysol. These datasets were upscaled to a coarser resolution of 5 km in the IFAS model to reduce the computational time for near-real-time forecasting.

Table 1. Land-use classification of the CRB and its surface tank parameter in the IFAS.

IFAS Parameters	GLCC Land-Use Class
1	Deciduous Broadleaf Forest Deciduous Needleleaf Forest Evergreen Broadleaf Forest Evergreen Needleleaf Forest Mixed Forest
2	Cropland/Grassland Mosaic Cropland/Woodland Mosaic Grassland Shrubland Mixed Shrubland/Grassland Savanna Barren or Sparsely Vegetated Herbaceous Tundra Wooded Wetland Mixed Tundra Bare Ground Tundra
3	Dryland Cropland and Pasture Irrigated Cropland and Pasture Mixed Dryland/Irrigated Cropland and Pasture Herbaceous Wetland Wooded Wetland
4	Urban and Built-Up Land
5	Water Bodies Snow or Ice

3.2. Satellite Precipitation Data

As discussed in the previous section, 97% of the CRB lies on the Indian side. Therefore, that area is considered to be ungauged due to the unavailability of data because of prolonged conflicts between Pakistan and India. However, satellite-based precipitation data, Global Satellite Mapping of Precipitation (GSMaP), were chosen as a replacement for rain gauge observations for hydrological simulation in the CRB. GSMaP is supported and developed by the Japan Science and Technology Agency (JST) and Japan Aerospace

Exploration Agency (JAXA) [62]. GSMaP incorporates data from both infrared (IR) and passive microwave (PMW) sensors, and its global scale spatial coverage is helpful in a wide range of hydrological applications. GSMaP provides many precipitation products globally, i.e., GSMaP-NOW (real-time), GSMaP-NRT (near-real-time), GSMaP-MVK (post-real-time microwave IR reanalyzed), and GSMaP-Gauge (gauge adjusted post-real-time). In this study, version 6 of the GSMaP-Gauge product was used (<ftp://hokusai.eorc.jaxa.jp/> accessed on 15 September 2022) after calibration with ground-based precipitation observations. GSMaP-Gauge has a temporal resolution of 1 h and a spatial resolution of $1^\circ \times 1^\circ$, covering the globe from 60°N to 60°S .

3.3. Chenab River Flow Data

The river flow data were obtained from Flood Forecasting Division, Pakistan Meteorological Department. Flow data were recorded every 6 h (at 00 h, 06 h, 12 h, and 18 h) during the monsoon season (15 June–15 September) at the first discharge gauging site, i.e., Marala Barrage, which is also known as the first rim station in Pakistan. The 2016 flood peak data were obtained and used to calibrate and validate the hydrologic model (Figure 2).

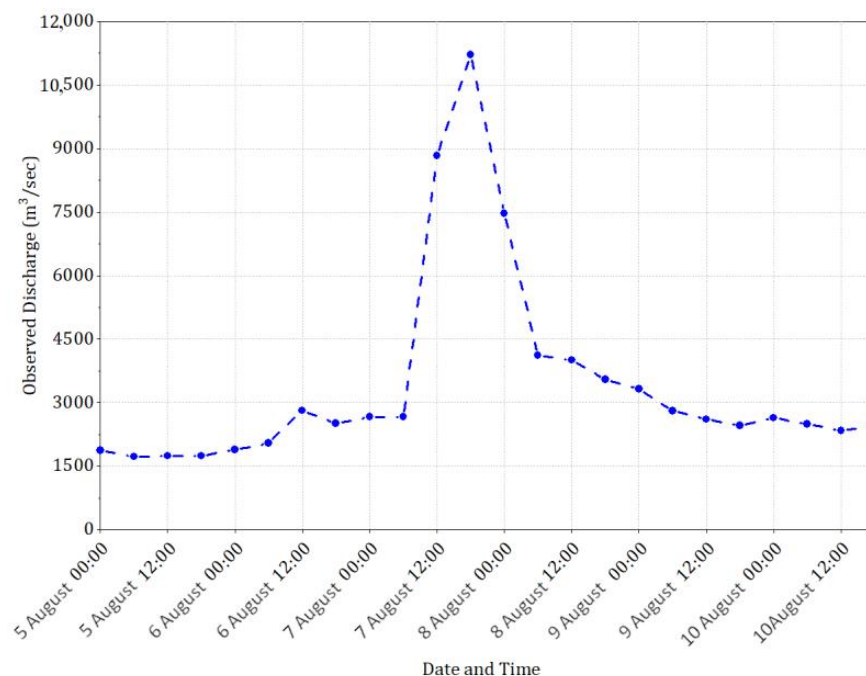


Figure 2. Six hourly observed flow rates (2016) at the Marala Barrage gauging site in Chenab River.

3.4. NWP Data for Flood Forecasting

In this study, NWP data were obtained from the Global Forecast System (GFS) from the Research Data Archive of the National Center for Atmospheric Research (NCAR), (<https://rda.ucar.edu/datasets/ds084.1/> accessed on 1 October 2022). The GFS is a global-scale NWP system that has a horizontal resolution of $0.25^\circ \times 0.25^\circ$ with 32 pressure levels. Data on these pressure levels are used to determine the initial and boundary conditions for large-scale atmospheric conditions without the assimilation of observational data. The GFS supplies forecasts with 16 days or 384 h of lead time. Forecasts are provided with 3 h intervals from a 0 h forecast (f00) to a 384 h forecast (f384). These forecasts are provided every 6 h, i.e., 00 h, 06 h, 12 h, and 18 h. In this study, GFS data were downloaded for the 2016 peak event in the CRB, i.e., 5th August–10th August, with up to 4 days of lead time or up to 96 h (f96) of forecast steps, as tabulated in Table 2. In the first step, the forecasts were downloaded after every 6 h for the first 30 h. In the second step, the forecasts were downloaded after every 12 h until 72 h, and in the end, one forecast after 96 h was downloaded to extract the precipitation data (Figure 3).

Table 2. Download pattern of GFS forecast files for the selected peak event in the CRB.

Lead Time		Downloaded GFS Files		
Days and Hours	Date	Time	Forecast Timestep (Hours)	
4 days	1 August 2016	00 UTC	96	
3 days	2 August 2016	00 UTC	72	
2 days 12 h	2 August 2016	12 UTC	60	
2 days	3 August 2016	00 UTC	48	
1 days 12 h	3 August 2016	18 UTC	30	
1 day	4 August 2016	00 UTC	24	
0 day 18 h	4 August 2016	06 UTC	18	
0 day 12 h	4 August 2016	12 UTC	12	
0 day 06 h	4 August 2016	18 UTC	06	

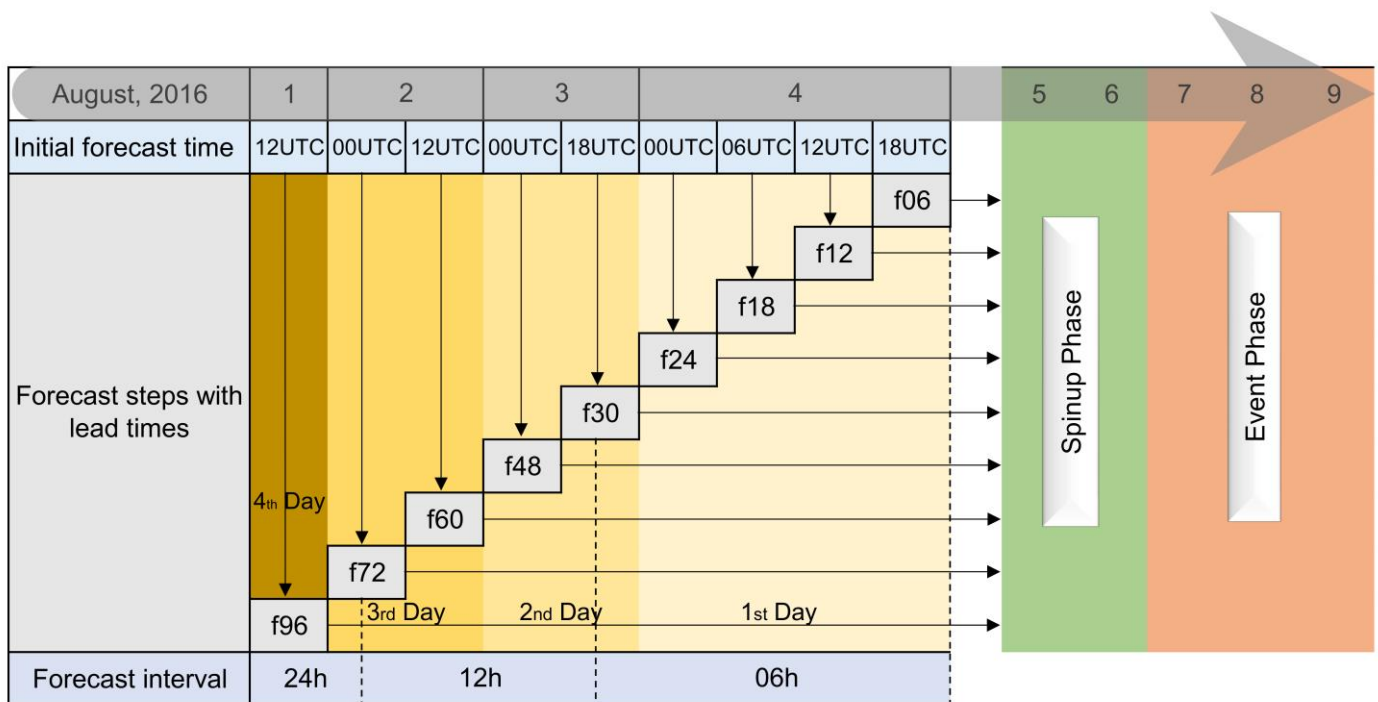


Figure 3. Graphical description of GFS data structure for selected peak event in the CRB.

3.5. WRF Model Settings for NWP Data

In this study, the NWP data were processed by using WRF version 4.0 with Advance Research WRF (ARW) dynamic core. The WRF model is a non-hydrostatic atmospheric model that was developed by the National Center for Atmospheric Research (NCAR), USA. This model is widely used for research, education, and real-time operational forecasting. It incorporates different physical processes for the representation of explicit microphysics, convection, surface physics, boundary layer turbulence, atmospheric radiation, surface temperature, and moisture at a sub-grid scale. The WRF-ARW model integrates compressible, non-hydrostatic Euler equations. The equations are cast in the flux form using variables that have conservation properties. These equations are governed by using a terrain-following, hydrostatic pressure vertical coordinate denoted by η and defined as:

$$\eta = \frac{P_d - P_t}{P_s - P_t} \tag{1}$$

where

P_d = the hydrostatic component of the pressure of dry air;

P_s and P_t = the values of P_d along the surface and top boundaries, respectively.

Since $\mu(x, y)$ represents the mass per unit area within the column in the model domain at (x, y) , the appropriate flux-form variables are as follows:

$$V = \mu v = (U, V, W), \quad (2)$$

$$\Omega = \mu \dot{\eta}, \quad (3)$$

$$\Theta_m = \mu \theta_m. \quad (4)$$

where

$v = (U, V, W)$ = the covariant velocities in the two horizontal and vertical directions;

$\dot{\eta} = \omega$ = the contravariant vertical velocity;

θ_m = is the moist potential temperature.

To solve the atmospheric dynamics in the WRF-ARW model, the flux-form Euler equation can be expressed as follows:

$$\partial_t U + (\nabla \cdot V_u) - (P\phi_n) + (P\phi_x) = F_U, \quad (5)$$

$$\partial_t V + (\nabla \cdot V_v) - \partial_y(P\phi_n) + (P\phi_y) = F_V, \quad (6)$$

$$\partial_t W + (\nabla \cdot V_w) - g(\partial_\eta P - \mu_d) = F_W, \quad (7)$$

$$\partial_t \Theta_m + (\nabla \cdot V \Theta_m) = F_{\Theta_m}, \quad (8)$$

$$\partial_t \mu_d + (\nabla \cdot V) = 0, \quad (9)$$

$$\partial_t \phi + \mu_d^{-1} [(V \cdot \nabla \phi) - gW] = 0. \quad (10)$$

The diagnostic equation for dry hydrostatic pressure:

$$\partial_t \phi = -\alpha_d \mu_d \quad (11)$$

The diagnostic relation for the full pressure (dry air plus water vapor):

$$P = P_o \left(\frac{R_d \Theta_m}{P_o \alpha_d} \right)^\gamma \quad (12)$$

In Equations (5)–(10), the subscripts x , y and η denote differentiation

$$\nabla \cdot V_a = \partial_x U_a - \partial_y V_a + \partial_\eta \Omega_a \quad (13)$$

and

$$\nabla \cdot V_a = U \partial_x a - V \partial_y a + \Omega \partial_\eta a \quad (14)$$

where

P = pressure;

a = generic variable;

γ = the ratio of heat capacities for dry air (c_p/c_v);

α_d = the inverse density of the dry air ($1/\rho_d$);

α = the inverse density taking the full parcel density into account;

R_d = the gas constant for dry air;

P_o = a reference surface pressure (in Pascals),

$\phi = gz$ = the non-conserved variables (geo-potential);

F_U , F_V , F_W , and F_{Θ_m} = forcing terms arising from model physics, turbulent mixing, spherical projections, and the Earth's rotation the inverse density of dry air, respectively.

Further description of the governing equations and processes can be found in the technical notes of WRF model version 4 [28].

WRF is used to dynamically downscale global forecasts to local or regional scales, as described by [63]. Many researchers, who have used regional models like WRF, have proposed some guidelines regarding the resolution, nesting strategies, and size of domains. For example, [64] concluded that, with a higher resolution (less than 5 km), the computational time required to perform physics on multiple domains in the WRF model was increased. In this study, the 5 km resolution of the final domain size was adopted to perform one-way and two-way nesting approaches in the CRB. The CRB was centered in the two domains, i.e., d01 and d02, as shown in Figure 4. The parent domain (d01) had dimensions of 2400 km (east–west) \times 1400 km (north–south), with a horizontal resolution of 25 km. The nested domain (d02) covered most of the area of Indian-Administered Jammu and Kashmir, in which 97% of the CRB lies. The horizontal resolution of d02 was 5 km, with dimensions of 480 km (east–west) \times 280 km (north–south). The WRF model has multiple applications with flexibility in the selection of physics and dynamics options. For each geographic location and application, there should be appropriate selections of WRF parameterizations. Therefore, in this research, the selections of physics options were based on previous studies in the region [46,65,66]. Complete information on the model’s physics options and configuration of grid description in the WRF model is tabulated in Table 3. It should be kept in mind that the cumulus scheme is theoretically only effective in bigger-sized domains (>10 km). Hence, the cumulus scheme was only used for d01, and d02 was set up without the cumulus scheme. Initial and boundary conditions were passed from d01 to d02. In this study, the one-way and two-way nesting approaches were selected to obtain downscaled NWP. The one-way nesting approach used no nesting of outer domain communication; the solution for the outer domain was independent of that of the nested domain. Alternatively, in two-way nesting, the solution on the outer domain was continually replaced by that of the nested domain.

Table 3. Summary of the WRF model grids configuration and physics options.

Model Aspects	Model Settings
Model version	4.0
Map projection	Lambert conformal
Mandatory Static Data	High-resolution dataset at 30'' and 6'' for d01 and d02, respectively
True-lat	33.27°N
True-lon	75.84°W
Domain grids	96 and 56 grid points for x and y, respectively
Domain ratio	1:5
Grid resolution	25 km (d01) and 5 km (d02)
Outer domain extent	2400 km \times 1400 km
Inner domain extent	480 km \times 280 km
Cloud microphysics	Lin (Purdue) [67]
Long-wave radiation	Rapid Radiative Transfer Model (RRTM) [68]
Short-wave radiation	Dudhia scheme [69]
Land surface model	Noah land surface model (LSM) [70]
Planetary boundary layer	Yonsei University scheme [71]
Cumulus parameterization	Kain–Fritsch [72] for d01; without cumulus scheme mode for d02

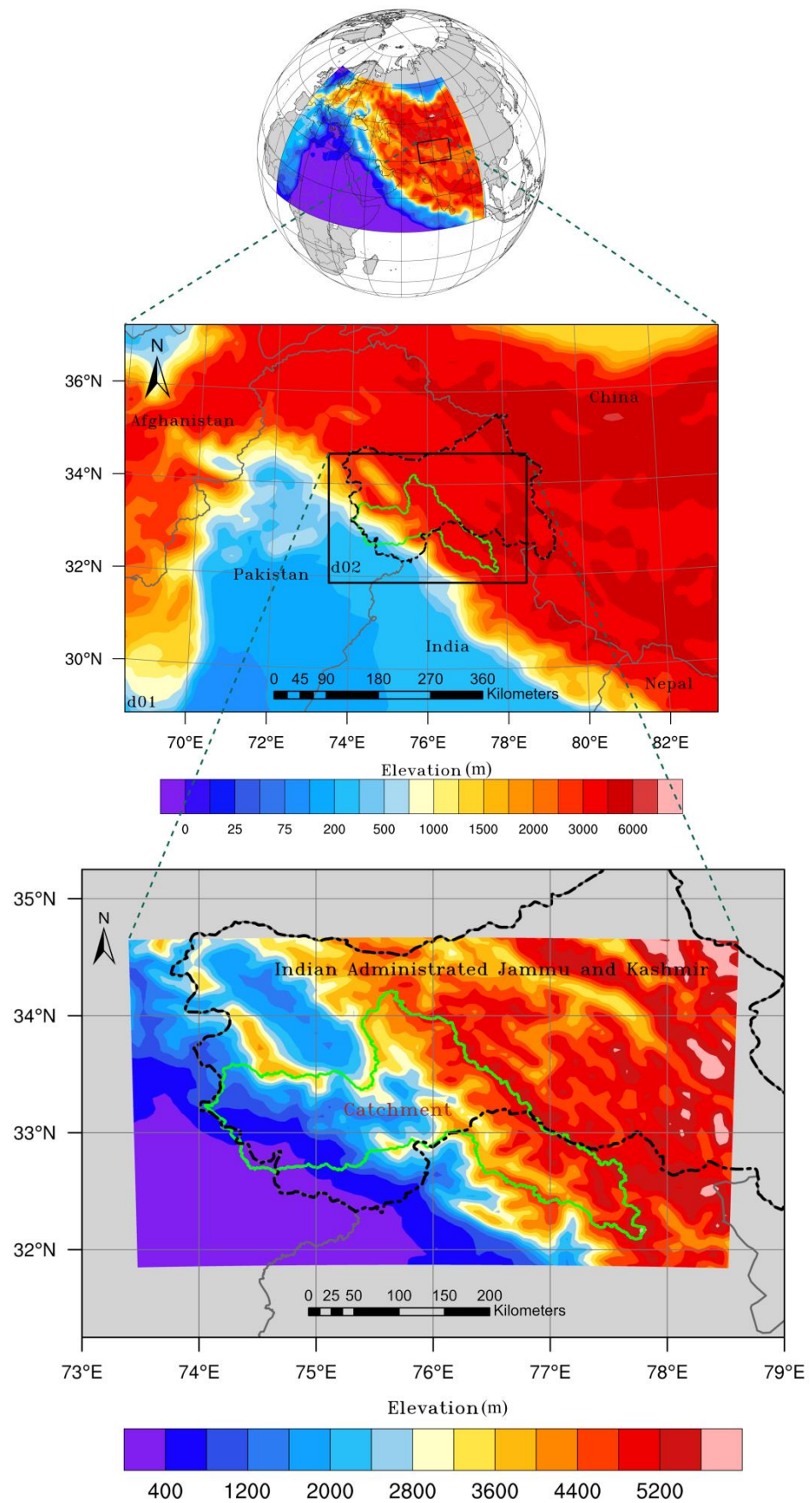


Figure 4. WRF model configuration with representation of domains and topography.

In the WRF pre-processing system, GFS data were interpolated onto the WRF grid. It has to be noted that GFS precipitation was not input to WRF, as it was solely derived by WRF physics and parametrizations itself. According to the objective of this study, to investigate the effect of lead time on NWP, GFS data with nine different lead times of up to 96 h were supplied to the WRF model to generate the precipitation forecasts, i.e., f06, f12, f18, f24, f30, f48, f60, f72, and f96. Forecast f06 means that the starting date and time of data acquisition was the 4th August 18 UTC, with the other terms following the same scheme (Figure 3). According to Figure 3, the 5th and 6th of August were considered to be the spin-up phase for the model to stabilize it, while the 7th to 9th were termed the event phase. Outcomes from every forecast run of the WRF model were converted into .asc files with Python routines for further use in the hydrological model.

3.6. Hydrologic Flood Simulation

Hydrological simulation in the CRB was conducted with the help of the IFAS model. This model was set up and applied in many previous studies to predict or simulate discharge in worldwide basins [41–44,73,74]. The IFAS model is a routing-based hydrologic model and a tank-based kinematic wave hydraulic model. It has several tank models, e.g., a surface tank model, an aquifer tank model, and a river tank model. It uses a non-linear relationship based on Manning's law, Darcey's law, and the kinematic wave equation to simulate the discharge in a stream. Further information can be found in the user manual of the IFAS model [75].

Topographic, land-use, and soil-type data were imported into the IFAS model to set up the model in the CRB. The IFAS model was set up with 6 hourly-based temporal resolutions and a spatial resolution of 5 km × 5 km. The IFAS model has a rainfall data manager, which was used to download and import the GSMaP-Gauge satellite rainfall data into the model. The downloaded GSMaP-Gauge rainfall data were supplied to calibrate the model for the 2016 flood event. To calibrate the model, sensitivity analysis was performed to tune the surface, aquifer, and river parameters. The simulated discharge at a river outlet (Marala Barrage) was validated with the observed discharge hydrograph.

The validated model was further used to predict the discharge in the CRB. The NWP rainfall from the global GFS model and the WRF model were supplied to the IFAS model to simulate the discharge with different lead times. According to Figure 3, forecasts up to 96 h (f96) were supplied to the model with different increments in forecast intervals. In the first step, the forecasts were supplied after every 6 h for the first 30 h. In the second step, the forecasts were supplied after every 12 h until 72 h, and in the end, one forecast after 96 h was supplied to the IFAS model (Figure 3). The hydrologic simulations of the global NWP, one-way, and two-way nesting approaches were compared, and their performance indices were calculated to indicate the performance of the best approach for forecast in the CRB. The coefficient of determination (R^2), the Nash–Sutcliffe efficiency (NSE), and PBIAS were used to evaluate the model performance in order to compare the forecasts in the CRB.

4. Results

4.1. Precipitation Forecasts from One-Way and Two-Way Nesting Approaches in WRF Model

In this study, the precipitation forecasts from the Global Forecasts System (GFS), with a resolution of 0.25° (~27.7 km), were downscaled to a 5 km resolution. The global GFS data were downscaled eighteen times at different forecast time-steps with the WRF one-way and two-way nesting methods. The precipitation from the global model, WRF one-way nesting, and WRF two-way nesting approaches were compared with each other to evaluate the hydrological and forecasting skills of GFS precipitation. Figure 5 displays the accumulated precipitation from 00:00 UTC 06 August 2016 to 18:00 UTC 07 August 2016 in the CRB. The accumulated total precipitations from the global GFS forecasts are displayed in the first column for each forecast step. The accumulated total precipitations from the one-way WRF nesting and the two-way WRF nesting are displayed with domain 1 (d01) and domain 2 (d02) in the second and fourth columns, respectively. All of the global GFS forecasts were

simulated by the WRF model with nine initial times between 18:00 UTC 4 August 2016 and 12:00 UTC 1 August 2016. These nine initial forecasts were from 06 h (f06) to 96 h (f96) with increments of 06 h, 12 h, and 24 h until f30, f72, and f96, respectively. It can be seen in Figure 5 that almost all of the forecast types showed a significant amount of precipitation inside the CRB. The global forecasts showed almost the same pattern of rainfall near or inside the CRB. However, the global forecasts and both d01 domains had coarser-resolution precipitation maps than the d02 precipitation maps. Moreover, d02 with the two-way nesting approach gave more detailed precipitation information than d02 with the one-way nesting approach. The domination trend of d02 with two-way nesting was observed for every forecast step. Summarized details of the precipitation maps are tabulated in Table 4, in which the accumulated total precipitation statistics for each forecast step and precipitation source are given. This table contains the average, maximum, minimum, and standard deviation of the total precipitation forecasts over the CRB. The trends show that the two-way nesting approach had high values of averages compared with the one-way nesting and global forecast approaches. It can also be seen that two-way nesting had larger standard deviation values than the one-way nesting and global forecast approaches, which shows that two-way nesting had better ability to capture the spatial variations in precipitation patterns than the one-way nesting and global forecast approaches. Global forecast, on the other hand, showed the smallest values of precipitation averages and standard deviations, which could make it poor for hydrological simulation in the CRB.

4.2. Flood Forecasts with Different Precipitation Sources, (i.e., Global, One-Way and Two-Way WRF Nesting Approaches)

To examine the applicability of global GFS precipitation, the GFS forecasts were processed and supplied to the calibrated IFAS model for flood forecasting. The different simulated peak discharges with different global forecasts for the 2016 flood event in the CRB are shown in Figure 6. It can be seen that simulations with GFS data underestimated the observed flood peaks for every forecast step because the simulated precipitation was too low, partly due to the coarse resolution of the mode. It could only reach a maximum of 5360 m³/s of discharge in all forecast steps, while the maximum observed peak discharge was recorded at 11,215 m³/s. To improve the accuracy of the forecasts, the coarser global forecasts were supplied to the WRF model to better resolve smaller-scale processes, leading to improved precipitation forecasts. The WRF model was run with the one-way and two-way nesting approaches, and the output of each WRF forecast, with d01 and d02, was then supplied to the calibrated IFAS model to observe the simulation patterns of each precipitation source and forecast step. Figure 6 also displays the hydrographs simulated with the precipitation of the one-way and two-way WRF nesting approaches. Here, lines with circle symbols represent the hydrologic simulation from the precipitation of the one-way nesting approach and lines with star symbols represent that of the two-way nesting approach. Figure 6 demonstrates that the downscaled precipitation showed more predictive skills of floods than the global GFS precipitation. It also shows that d01 and d02 from the one-way nesting approach overestimated the observed hydrograph in almost all of the forecast steps for the 2016 flood event in the CRB. Moreover, d01 (one-way nesting) showed an irregular and overestimated discharge pattern compared with the observed hydrograph, while the hydrograph with the precipitation of d02 (one-way nesting) presented improvements over d01 (one-way nesting). However, d02 (one-way nesting) was also unable to capture the shape of the observed hydrograph very well. Six out of nine forecasts with d01 (one-way nesting) overestimated the observed peak discharge. d01 and d02 with two-way nesting displayed more promising results for flood forecasting in the CRB than one-way nesting (Figure 6). Most of the flood hydrographs were in good shape and well-captured the peak event, except f72. This was due to the shifting of the precipitation forecast (f72) to the southern side of the CRB, as displayed in Figure 5. Seven out of nine forecasts were able to capture the 2016 flood event in the CRB. These

forecasts were able to predict precipitation within the CRB with an accurate intensity and were thus successful in predicting the exceptionally high flood peak event.

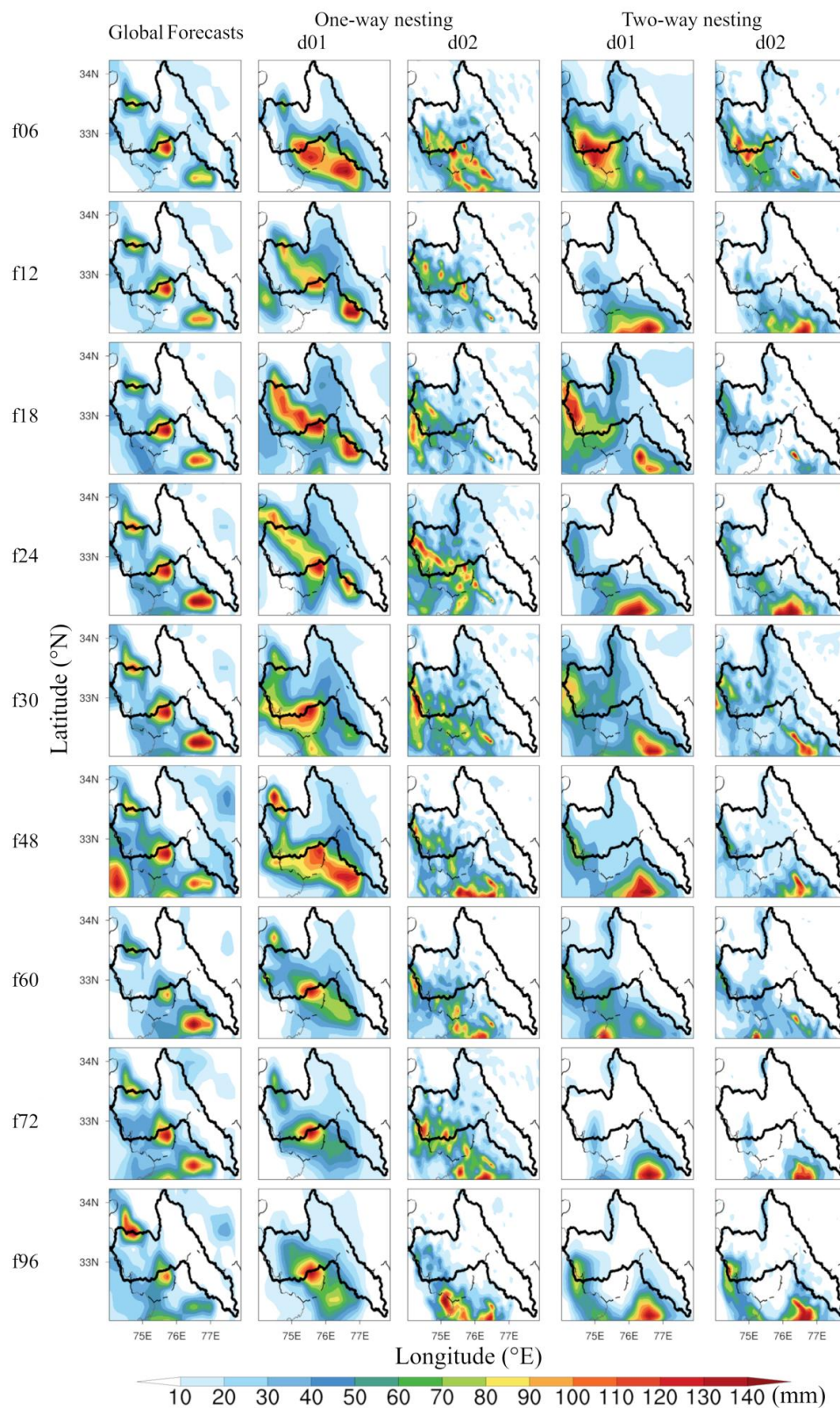


Figure 5. Spatial distribution of GFS and WRF downscaled accumulated precipitation (mm) from 00:00 UTC 06 August 2016 to 18:00 UTC 07 August 2016. The forecast lead times are shown on the left, and the experiment type is shown at the top.

Table 4. Average (avg), minimum (min), maximum (max), and standard deviation (std) for the global GFS, one-way and two-way WRF simulated accumulated precipitation (from 00:00 UTC 06 August to 18:00 UTC 07 August 2016).

Forecasts		f06	f12	f18	f24	f30	f48	f60	f72	f96
Global forecast	avg	19.5	18.6	21.1	21.9	23.7	32.5	30.4	28.2	21.3
	max	142.6	132.1	147.4	136.0	152.9	142.2	213.2	160.8	134.9
	min	0.0	0.0	0.0	0.1	0.1	0.0	0.0	0.1	0.0
	std	18.7	18.7	22.0	24.1	25.3	26.3	30.6	25.9	19.6
One-way nesting (d02)	avg	57.0	45.0	48.5	53.9	61.6	68.6	57.1	63.5	76.1
	max	378.8	397.0	369.8	290.8	354.7	477.6	444.0	409.5	746.0
	min	1.4	0.3	0.1	0.4	0.2	0.5	0.5	0.2	0.0
	std	66.6	51.5	53.5	50.9	61.2	75.9	69.8	70.5	114.1
Two-way nesting (d02)	avg	171.0	141.8	98.1	147.8	118.0	141.9	115.5	123.6	165.8
	max	1268.5	1650.2	1029.5	1371.3	807.0	1440.2	1131.3	1826.5	1298.3
	min	3.0	0.0	0.1	0.0	1.3	0.0	0.2	0.0	0.0
	std	187.1	217.9	98.7	209.0	109.4	168.2	126.4	219.4	229.0

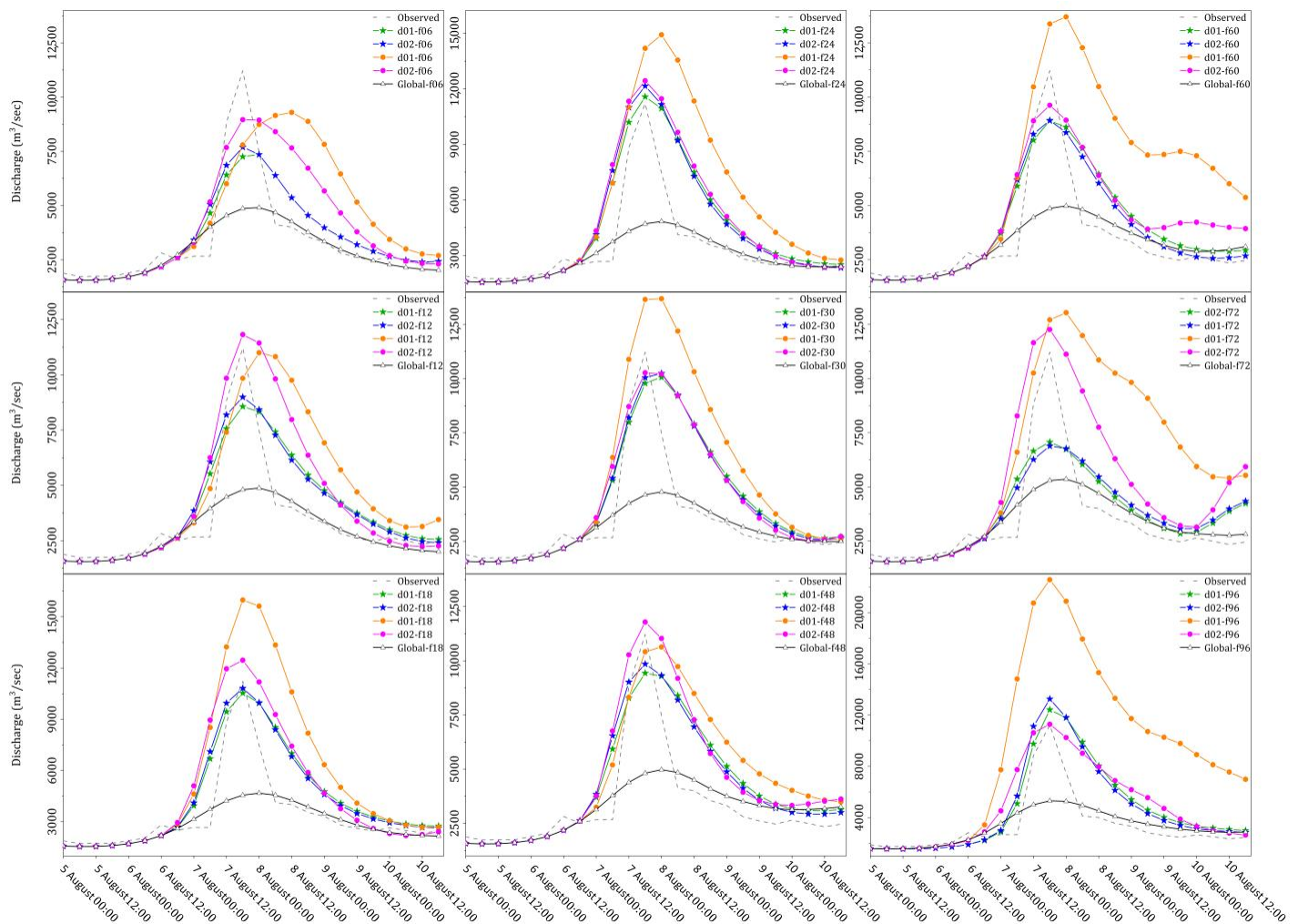


Figure 6. Observed vs simulated flood hydrographs driven by different precipitation sources and different initial forecasts times (i.e., f06, f12, f18, f24, f30, f48, f60, f72, and f96) for the 2016 event in the CRB. The circle symbol represents one-way nesting, and the star symbol represents two-way nesting.

4.3. Hydrologic Performance Evaluation of WRF Domains

In this section, the hydrological skills of two domains in the WRF model (d01 and d02), with one-way and two-way nesting, were evaluated with performance indices, e.g., R^2 , NSE, and PBIAS [76–78]. R^2 is the coefficient of determination, ranging from 0 to 1, which was used to depict the strength of linear correlation between observed and simulated discharge (Equation (15)). NSE is the Nash–Sutcliffe Efficiency, falling between $-\infty$ and 1, which was used to define how perfectly the observed and modeled discharge matched the 1:1 line (Equation (16)). PBIAS was used to capture the underestimation or overestimation of simulated values relative to observed values; PBIAS shows a value of 0 under optimal conditions, whereas a positive value denotes an underestimation and a negative denotes an overestimation (Equation (17)). Figure 7 displays the performance indices of the simulated discharge driven by the IFAS model for different forecast steps during the 2016 peak event in the CRB. The scatter plots of six hourly-based observed versus simulated discharge rates at different forecast steps are also presented in Figure 7. It can be seen in the figure that the simulations with precipitation from the one-way nesting approach showed more underestimation, with high values of PBIAS, than simulations with global forecasts and precipitation from the two-way nesting approach for all forecast steps. Simulations with one-way nesting data also showed poor performance for both domains, with low values of NSE, compared with simulations with global forecasts and precipitation from the two-way nesting approach. In most of the forecast steps, observed and simulated discharge also showed lower coefficients of determination for simulation with one-way nesting data than for simulations with data derived from the two-way nesting approach. The simulations with global forecast data displayed lower R^2 and NSE values between observed and simulated values than simulations with two-way nesting data for almost all of the forecast steps. The simulations with global forecast data showed a good hydrograph shape according to Figure 7, but they could not precisely capture the peaks, as discussed earlier. Hence, it can be stated that d02 (two-way nesting) exhibited the best performance in simulating the forecasts among all of the precipitation sources, with higher R^2 and NSE values and acceptable limits of PBIAS. The simulations with d02 (two-way nesting) displayed high values of R^2 (f06 = 0.75, f12 = 0.75, f18 = 0.78, f24 = 0.79, f30 = 0.7, f48 = 0.74, f60 = 0.76, f72 = 0.67, and f96 = 0.84), high values of NSE (f06 = 0.75, f12 = 0.67, f18 = 0.5, f24 = 0.3, f30 = 0.42, f48 = 0.54, f60 = 0.71, f72 = 0.65, and f96 = 0.26), and low values of PBIAS (f06 = 3.5%, f12 = 15.9%, f18 = 26.5%, f24 = 31.3%, f30 = 25.3%, f48 = 24.2%, f60 = 12.8%, f72 = 7.1%, and f96 = 34.4%) compared with simulations with one-way nesting and global forecast data.

$$R^2 = \frac{\sum_{i=1}^n (O_i - \bar{O}) \cdot (S_i - \bar{S})}{\sqrt{\sum_{i=1}^n (O_i - \bar{O})^2} \cdot \sqrt{\sum_{i=1}^n (S_i - \bar{S})^2}} \quad (15)$$

$$NSE = 1 - \left[\frac{\sum_{i=1}^n (O_i - S_i)^2}{\sum_{i=1}^n (O_i - \bar{O})^2} \right] \quad (16)$$

$$PBIAS = \frac{\sum_{i=1}^n (S_i - O_i)}{\sum_{i=1}^n O_i} \times 100 \quad (17)$$

where O_i , \bar{O} , S_i , and \bar{S} represent the observed discharge, average observed discharge, simulated discharge, and average simulated discharge, respectively.

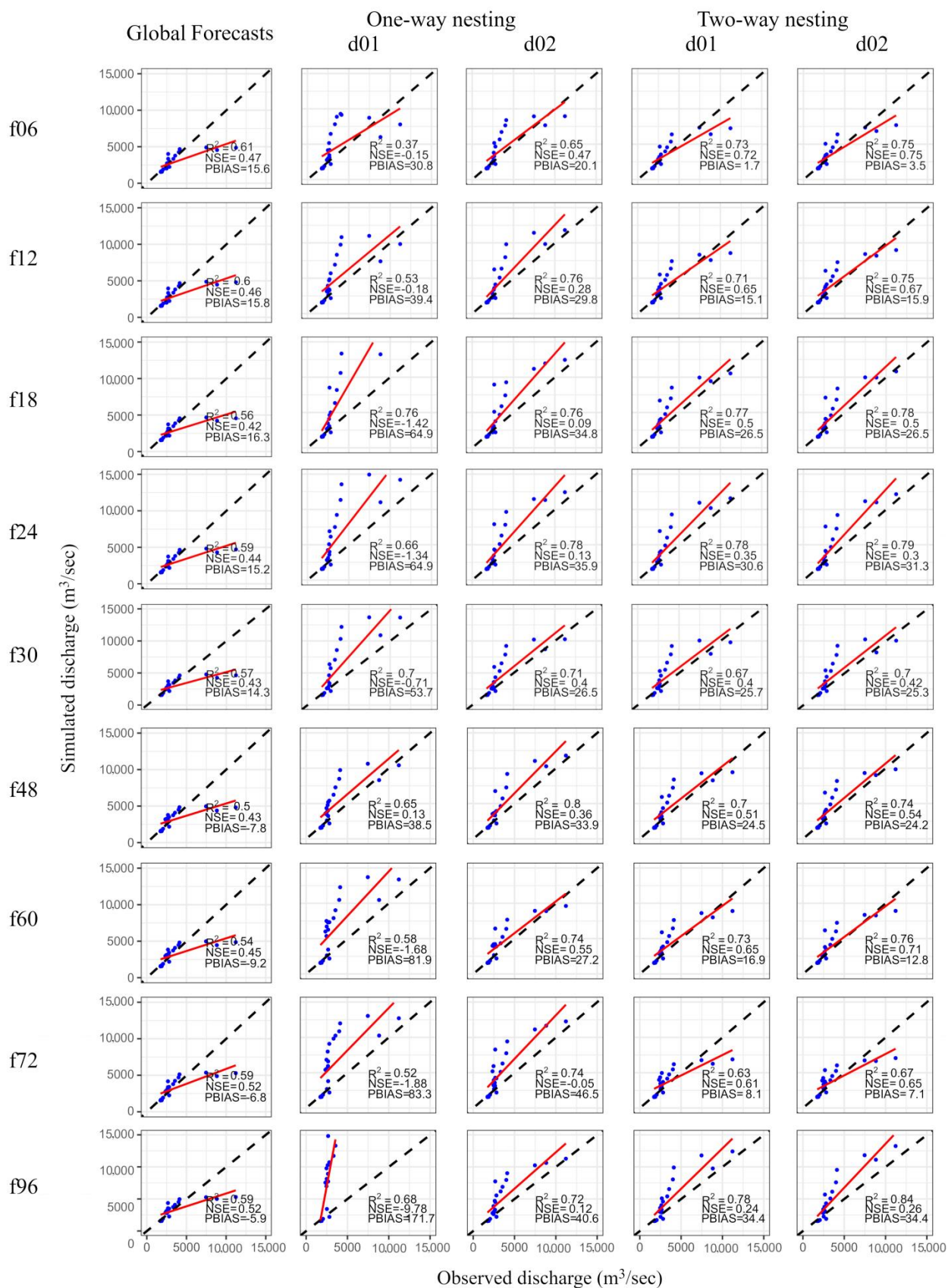


Figure 7. Scatter plot and performance evaluation indices (R², NSE, and PBIAS) of simulated flows driven by the global, one-way nesting, and two-way nesting WRF approaches.

For comparison between simulations with data from the two domains, i.e., d01 and d02, radar plots were also plotted for R^2 , NSE, and PBIAS, as displayed in Figure 8. In these plots, simulations with data from d01 and d02 with the one-way and two-way nesting approaches were separately compared. It can be seen in Figure 8 that simulations with data from d01 (one-way nesting) exhibited poorer performance than simulations with data from d01 (two-way nesting). For example, when switching from simulations with data from one-way nesting to simulations with two-way nesting data for d01(f06), the values of R^2 , NSE, and PBIAS improved from 0.37 to 0.73, -0.15 to 0.72 , and 30.8 to 1.7 , respectively. Similar improvements were observed for the rest of the forecast steps. In the case of simulations with data from d01 (one-way nesting), the f96 forecast heavily overestimated the observed discharge, and its values of NSE and PBIAS were very low and very high, respectively, compared with the other forecast steps. However, the f96 forecast showed a good performance for simulations with data from the d01 (two-way nesting) case with high NSE and acceptable PBIAS values. In the second column of Figure 8, the radar plots of the performance statistics of simulations with data from d02 with the one-way and two-way nesting approaches are displayed. Radar plots for simulations with data from d02 with the one-way and two-way nesting approaches depict the same behavior as d01. Similarly, when switching from simulations applying data with one-way nesting to simulations with data using two-way nesting for d02(f06), the values of R^2 , NSE, and PBIAS improved from 0.65 to 0.75 , 0.47 to 0.75 , and 20.1 to 3.5 , respectively. The rest of the forecast steps also showed that the simulations with data from d02 (two-way nesting) outperformed the simulations with data from d02 (one-way nesting) in all of the statistical calculations.

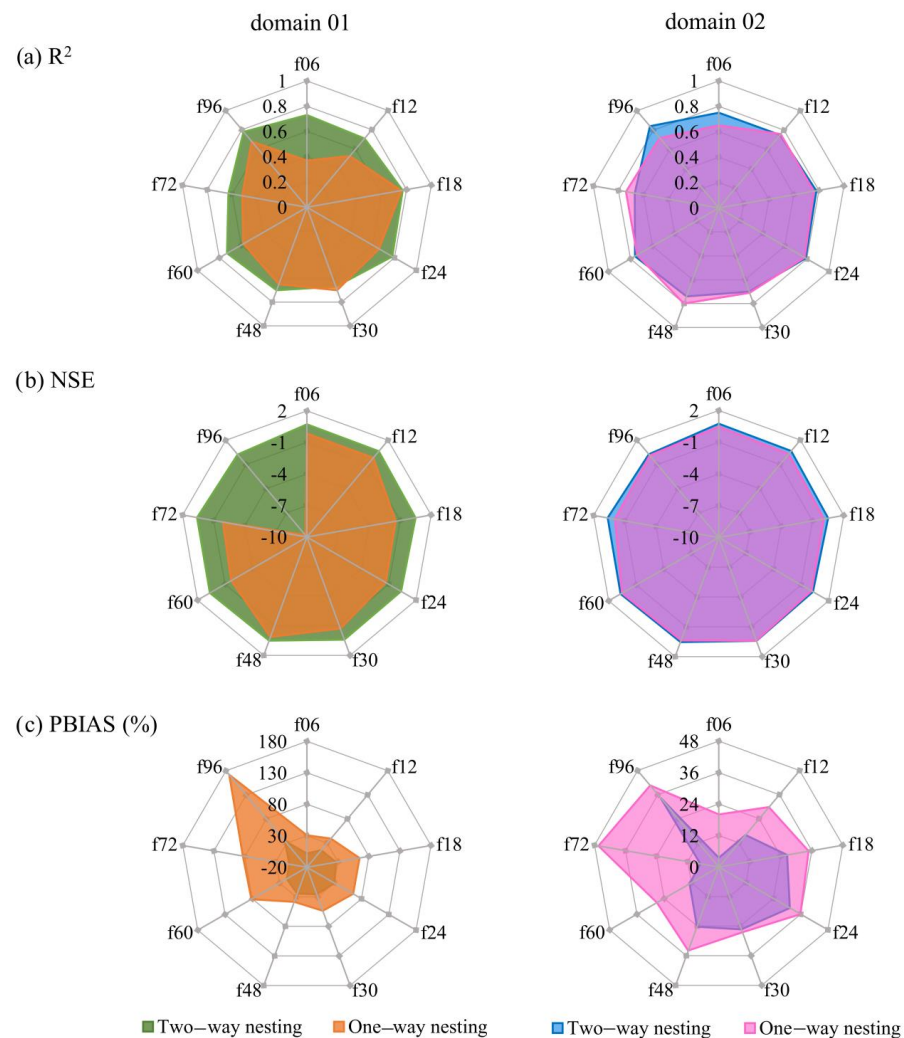


Figure 8. Radar plots of performance indices.

In the conclusion, the two-way WRF nesting approach showed a higher agreement with observations in producing precipitation and when data were used to simulate hydrographs compared with the global forecast and one-way WRF nesting approaches. Therefore, two-way nesting was better than one-way nesting for providing precipitation data when capturing the 2016 flood peak in the CRB. The two-way WRF nesting approach produced improvements in both the precipitation and hydrologic simulations applying the precipitation data compared with the one-way WRF nesting approach; this was consistent with other studies [79,80].

5. Discussion and Conclusions

Flood forecasting and simulation are major problems in large transboundary catchments, especially in the India–Pakistan region where data sharing is a major problem due to the Jammu and Kashmir conflict. Pakistan does not have access to in situ rain gauge stations on the Indian side of Jammu and Kashmir. However, Pakistan has faced many floods in the recent past due to climate change and heavy monsoonal rainfalls. Recently, several satellite products and numerical weather prediction models became available to estimate or predict atmospheric variables, including precipitation information. This study was used to evaluate the performance of the Weather Research and Forecast (WRF) model for precipitation forecasting in the transboundary Chenab River Basin (CRB) in Pakistan. About 97% of the CRB, above the first gauging site (Marala Barrage in Pakistan), lies on the Indian side of Jammu and Kashmir, where ground data acquisition is a critical job. Hence, in this study, a combination of precipitation from the gauge-calibrated Global Satellite Mapping of Precipitation (GSMaP_Gauge) and the numerical weather prediction (NWP) precipitation from the WRF model was used to predict the forecast of the Chenab River for the 2016 flood event.

First of all, GSMaP_Gauge was used to calibrate the Integrated Flood Analysis System (IFAS) model of the 2016 flood event in the CRB. Later, NWP precipitation, obtained from the Global Forecast System (GFS) model, was used in the calibrated IFAS model to predict the flood peak with different precipitation forecast lead times. The forecasts were used every 6 h for the first 30 h, then every 12 h until 72 h, and then every 24 h until 96 h to predict the flood event in the IFAS model. The GFS precipitation-based simulations underestimated the observed hydrograph for every forecast step, (i.e., f06, f12, f18, f24, f30, f48, f60, f72, and f96) because the coarser resolution of the global GFS forecasts could not properly predict the intensities of precipitation. The global precipitation forecasts were downscaled with WRF. In this study, the CRB was centered in two domains, i.e., d01 and d02, in the WRF model. The one-way and two-way nesting approaches were selected to generate better precipitation forecasts and hydrological simulations. As the spatial resolution of precipitation forecasts (i.e., f06, f12, f18, f24, f30, f48, f60, f72, and f96) became finer (with WRF nesting), the agreement of simulated hydrograph with observed hydrograph significantly increased and the flood hydrographs, simulated with one-way and two-way nesting precipitation, showed improvements in capturing the 2016 flood peak compared with simulations with the GFS forecasts.

Simulations with the d01 and d02 domains were also separately compared to obtain the optimal flood forecast in the Chenab River. It was observed that simulations with precipitation from d01 and d02 with the one-way nesting approach overestimated the observed hydrograph in almost all of the forecast steps for the 2016 flood event in the Chenab River. Simulations with data derived from the one-way nesting approach were unable to properly capture the shape of the observed hydrograph. The simulations applying data from d01 and d02, with the two-way nesting approach, displayed more promising results for flood forecasting in the CRB than the simulations with precipitation using the one-way nesting approach. Most of the flood hydrographs were in strong shape and adequately captured the peak event. Seven out of nine forecasts were able to reproduce the 2016 flood event in the CRB. These forecasts were able to predict precipitation within the CRB with accurate intensity and were thus successful in predicting the exceptionally

high flood peak event. Performance indices showed that the simulated hydrographs, with precipitation from two-way WRF nesting, at different lead times showed remarkable results compared with the observed hydrographs, with the highest R2 and NSE values and the lowest PBIAS values. As a conclusive note, it can be said applying the precipitation from two-way WRF nesting enabled the simulation of flood hydrograph with a remarkable lead time of 96 h with coupled hydrometeorological flow simulation.

Although this study was only focused on the 2016 flood event in the CRB, it clearly shows that two-way coupled atmospheric–hydrological flow simulation calibrated with satellite products and run with NWP precipitation has the potential to improve precipitation and hydrological forecasts with a sufficient lead time. It can also be useful in the issuance of early warnings to initiate necessary precautions, timely emergency response, and public evacuation before a catastrophic flood event. However, further studies need to be conducted to verify this approach with different WRF domain sizes, different combinations of WRF parameterization schemes (e.g., cumulus and microphysics), and different flood events.

Author Contributions: Conceptualization, E.A.; methodology, E.A. and N.S.; software, E.A. and M.R.A.; validation, E.A. and F.A.J.; formal analysis, E.A. and M.R.A.; data curation, N.S. and A.S.; writing—original draft preparation, E.A.; writing—review and editing, A.S. and K.B.; visualization, K.B. and P.K.; supervision, P.K. All authors have read and agreed to the published version of the manuscript.

Funding: This research received no external funding.

Data Availability Statement: No new data were created or analyzed in this study. Data sharing is not applicable to this article.

Acknowledgments: The authors are thankful to the GSMAp research community for making the satellite precipitation data available for this study. The authors would like to extend their gratitude to the Flood Forecasting Division, Pakistan Meteorological Department (PMD), for the provision of valuable data for this research. E.A. is grateful to the Higher Education Commission of Pakistan (HEC) and the German Academic Exchange Service (DAAD) for providing him a scholarship opportunity to pursue his Ph.D. research. E.A. is thankful for the support of the Graduate Academy of TU Dresden for the completion and wrap-up phase of the Ph.D. grant. E.A. would also like to thank the facilities provided by the Institute of Urban and Industrial Water Management, TU Dresden.

Conflicts of Interest: The authors declare no conflict of interest.

References

1. Saddique, N.; Muzammil, M.; Jahangir, I.; Sarwar, A.; Ahmed, E.; Aslam, R.A.; Bernhofer, C. Hydrological evaluation of 14 satellite-based, gauge-based and reanalysis precipitation products in a data-scarce mountainous catchment. *Hydrol. Sci. J.* **2022**, *67*, 436–450. [[CrossRef](#)]
2. Larson, L.W.; Peck, E.L. Accuracy of precipitation measurements for hydrologic modeling. *Water Resour. Res.* **1974**, *10*, 857–863. [[CrossRef](#)]
3. Sun, Q.; Miao, C.; Duan, Q.; Ashouri, H.; Sorooshian, S.; Hsu, K. A Review of Global Precipitation Data Sets: Data Sources, Estimation, and Intercomparisons. *Rev. Geophys.* **2018**, *56*, 79–107. [[CrossRef](#)]
4. Parvaze, S.; Khan, J.N.; Kumar, R.; Allaie, S.P. Flood forecasting in Jhelum river basin using integrated hydrological and hydraulic modeling approach with a real-time updating procedure. *Clim. Dyn.* **2022**, *59*, 2231–2255. [[CrossRef](#)]
5. Abro, M.I.; Zhu, D.; Ali Khaskheli, M.; Elahi, E.; Aleem ul Hassan Ramay, M. Statistical and qualitative evaluation of multi-sources for hydrological suitability inflood-prone areas of Pakistan. *J. Hydrol.* **2020**, *588*, 125117. [[CrossRef](#)]
6. Yucel, I. Assessment of a flash flood event using different precipitation datasets. *Nat. Hazards* **2015**, *79*, 1889–1911. [[CrossRef](#)]
7. Yilmaz, K.K.; Hogue, T.S.; Hsu, K.; Sorooshian, S.; Gupta, H.V.; Wagener, T. Intercomparison of Rain Gauge, Radar, and Satellite-Based Precipitation Estimates with Emphasis on Hydrologic Forecasting. *J. Hydrometeorol.* **2005**, *6*, 497–517. [[CrossRef](#)]
8. Chen, Y.; Ebert, E.E.; Walsh, K.J.E.; Davidson, N.E. Evaluation of TRMM 3B42 precipitation estimates of tropical cyclone rainfall using PACRAIN data. *J. Geophys. Res. Atmos.* **2013**, *118*, 2184–2196. [[CrossRef](#)]
9. Maddah, M.A.; Akhoond-Ali, A.M.; Ahmadi, F.; Ghafarian, P.; Rusin, I.N. Forecastability of a heavy precipitation event at different lead-times using WRF model: The case study in Karkheh River basin. *Acta Geophys.* **2021**, *69*, 1979–1995. [[CrossRef](#)]
10. Dubey, A.K.; Kumar, P.; Chembolu, V.; Dutta, S.; Singh, R.P.; Rajawat, A.S. Flood modeling of a large transboundary river using WRF-Hydro and microwave remote sensing. *J. Hydrol.* **2021**, *598*, 126391. [[CrossRef](#)]

11. Kidd, C.; Becker, A.; Huffman, G.J.; Muller, C.L.; Joe, P.; Skofronick-Jackson, G.; Kirschbaum, D.B. So, How Much of the Earth's Surface Is Covered by Rain Gauges? *Bull. Am. Meteorol. Soc.* **2017**, *98*, 69–78. [[CrossRef](#)] [[PubMed](#)]
12. Nkuna, T.R.; Odiyo, J.O. Filling of missing rainfall data in Luvuvhu River Catchment using artificial neural networks. *Phys. Chem. Earth Parts A/B/C* **2011**, *36*, 830–835. [[CrossRef](#)]
13. Biswas, N.K.; Hossain, F.; Bonnema, M.; Aminul Haque, A.M.; Biswas, R.K.; Bhuyan, A.; Hossain, A. A computationally efficient flash flood early warning system for a mountainous and transboundary river basin in Bangladesh. *J. Hydroinformatics* **2020**, *22*, 1672–1692. [[CrossRef](#)]
14. Joyce, R.J.; Janowiak, J.E.; Arkin, P.A.; Xie, P. CMORPH: A Method that Produces Global Precipitation Estimates from Passive Microwave and Infrared Data at High Spatial and Temporal Resolution. *J. Hydrometeorol.* **2004**, *5*, 487–503. [[CrossRef](#)]
15. Hong, Y.; Hsu, K.-L.; Sorooshian, S.; Gao, X. Precipitation Estimation from Remotely Sensed Imagery Using an Artificial Neural Network Cloud Classification System. *J. Appl. Meteorol.* **2004**, *43*, 1834–1853. [[CrossRef](#)]
16. Garstang, M.; Kummerow, C.D. The Joanne Simpson Special Issue on the Tropical Rainfall Measuring Mission (TRMM). *J. Appl. Meteorol.* **2000**, *39*, 1961. [[CrossRef](#)]
17. Hou, A.Y.; Kakar, R.K.; Neeck, S.; Azarbarzin, A.A.; Kummerow, C.D.; Kojima, M.; Oki, R.; Nakamura, K.; Iguchi, T. The Global Precipitation Measurement Mission. *Bull. Am. Meteorol. Soc.* **2014**, *95*, 701–722. [[CrossRef](#)]
18. Okamoto, K.I.; Ushio, T.; Iguchi, T.; Takahashi, N.; Iwanami, K. The global satellite mapping of precipitation (GSMaP) project. In Proceedings of the 2005 IEEE International Geoscience and Remote Sensing Symposium, 2005. IGARSS'05, Seoul, Korea, 29 July 2005; IEEE: Manhattan, NY, USA, 2005; Volume 5, pp. 3414–3416.
19. Chang, M.-J.; Chang, H.-K.; Chen, Y.-C.; Lin, G.-F.; Chen, P.-A.; Lai, J.-S.; Tan, Y.-C. A Support Vector Machine Forecasting Model for Typhoon Flood Inundation Mapping and Early Flood Warning Systems. *Water* **2018**, *10*, 1734. [[CrossRef](#)]
20. Wagena, M.B.; Goering, D.; Collick, A.S.; Bock, E.; Fuka, D.R.; Buda, A.; Easton, Z.M. Comparison of short-term streamflow forecasting using stochastic time series, neural networks, process-based, and Bayesian models. *Environ. Model. Softw.* **2020**, *126*, 104669. [[CrossRef](#)]
21. Diez-Sierra, J.; del Jesus, M. Long-term rainfall prediction using atmospheric synoptic patterns in semi-arid climates with statistical and machine learning methods. *J. Hydrol.* **2020**, *586*, 124789. [[CrossRef](#)]
22. Paul, R.K.; Paul, A.K.; Bhar, L.M. Wavelet-based combination approach for modeling sub-divisional rainfall in India. *Theor. Appl. Climatol.* **2020**, *139*, 949–963. [[CrossRef](#)]
23. Zhang, X.; Anagnostou, E.N.; Frediani, M.; Solomos, S.; Kallos, G. Using NWP Simulations in Satellite Rainfall Estimation of Heavy Precipitation Events over Mountainous Areas. *J. Hydrometeorol.* **2013**, *14*, 1844–1858. [[CrossRef](#)]
24. Liu, J.; Wang, J.; Pan, S.; Tang, K.; Li, C.; Han, D. A real-time flood forecasting system with dual updating of the NWP rainfall and the river flow. *Nat. Hazards* **2015**, *77*, 1161–1182. [[CrossRef](#)]
25. Schmidli, J.; Goodess, C.M.; Frei, C.; Haylock, M.R.; Huntecha, Y.; Ribalaygua, J.; Schmith, T. Statistical and dynamical downscaling of precipitation: An evaluation and comparison of scenarios for the European Alps. *J. Geophys. Res.* **2007**, *112*, D04105. [[CrossRef](#)]
26. Vichot-Llano, A.; Martinez-Castro, D.; Giorgi, F.; Bezanilla-Morlot, A.; Centella-Artola, A. Comparison of GCM and RCM simulated precipitation and temperature over Central America and the Caribbean. *Theor. Appl. Climatol.* **2021**, *143*, 389–402. [[CrossRef](#)]
27. Noble, E.; Druyan, L.M.; Fulakeza, M. The Sensitivity of WRF Daily Summertime Simulations over West Africa to Alternative Parameterizations. Part II: Precipitation. *Mon. Weather Rev.* **2017**, *145*, 215–233. [[CrossRef](#)]
28. Skamarock, W.C.; Klemp, J.B.; Dudhia, J.; Gill, D.O.; Liu, Z.; Berner, J.; Wang, W.; Powers, J.G.; Duda, M.G.; Barker, D.M.; et al. *A Description of the Advanced Research WRF Model Version 4*; National Center for Atmospheric Research: Boulder, CO, USA, 2019; p. 145.
29. Skamarock, W.C.; Klemp, J.B. A time-split nonhydrostatic atmospheric model for weather research and forecasting applications. *J. Comput. Phys.* **2008**, *227*, 3465–3485. [[CrossRef](#)]
30. Molteni, F.; Buizza, R.; Palmer, T.N.; Petroliagis, T. The ECMWF Ensemble Prediction System: Methodology and validation. *Q. J. R. Meteorol. Soc.* **1996**, *122*, 73–119. [[CrossRef](#)]
31. Black, T.L. The New NMC Mesoscale Eta Model: Description and Forecast Examples. *Weather Forecast.* **1994**, *9*, 265–278. [[CrossRef](#)]
32. Saito, K.; Fujita, T.; Yamada, Y.; Ishida, J.; Kumagai, Y.; Aranami, K.; Ohmori, S.; Nagasawa, R.; Kumagai, S.; Muroi, C.; et al. The Operational JMA Nonhydrostatic Mesoscale Model. *Mon. Weather Rev.* **2006**, *134*, 1266–1298. [[CrossRef](#)]
33. Zechun, L.; Dehui, C. The development and application of the operational ensemble prediction system at National Meteorological Center. *J. Appl. Meteorol. Sci.* **2002**, *13*, 1–15.
34. Yang, W.; Brüggemann, K.; Seguya, K.D.; Ahmed, E.; Kaeseberg, T.; Dai, H.; Hua, P.; Zhang, J.; Krebs, P. Measuring performance of low impact development practices for the surface runoff management. *Environ. Sci. Ecotechnology* **2020**, *1*, 100010. [[CrossRef](#)]
35. Yan, H.; Gallus, W.A. An Evaluation of QPF from the WRF, NAM, and GFS Models Using Multiple Verification Methods over a Small Domain. *Weather Forecast.* **2016**, *31*, 1363–1379. [[CrossRef](#)]
36. Yu, W.; Nakakita, E.; Kim, S.; Yamaguchi, K. Impact Assessment of Uncertainty Propagation of Ensemble NWP Rainfall to Flood Forecasting with Catchment Scale. *Adv. Meteorol.* **2016**, *2016*, 1384302. [[CrossRef](#)]
37. Roberts, N.M.; Cole, S.J.; Forbes, R.M.; Moore, R.J.; Boswell, D. Use of high-resolution NWP rainfall and river flow forecasts for advance warning of the Carlisle flood, north-west England. *Meteorol. Appl.* **2009**, *16*, 23–34. [[CrossRef](#)]

38. Ushiyama, T.; Sayama, T.; Tatebe, Y.; Fujioka, S.; Fukami, K. Numerical Simulation of 2010 Pakistan Flood in the Kabul River Basin by Using Lagged Ensemble Rainfall Forecasting. *J. Hydrometeorol.* **2014**, *15*, 193–211. [[CrossRef](#)]
39. Politi, N.; Vlachogiannis, D.; Sfetsos, A.; Nastos, P.T. High-resolution dynamical downscaling of ERA-Interim temperature and precipitation using WRF model for Greece. *Clim. Dyn.* **2021**, *57*, 799–825. [[CrossRef](#)]
40. Sugiura, T.; Fukami, K.; Inomata, H. Development of Integrated Flood Analysis System (IFAS) and Its Applications. In Proceedings of the World Environmental and Water Resources Congress, Honolulu, HI, USA, 12–16 May 2008; American Society of Civil Engineers: Reston, VA, USA, 2008; pp. 1–10.
41. Sugiura, A.; Fujioka, S.; Nabesaka, S.; Tsuda, M.; Iwami, Y. Development of a flood forecasting system on the upper Indus catchment using IFAS. *J. Flood Risk Manag.* **2016**, *9*, 265–277. [[CrossRef](#)]
42. Hafiz, I.; Nor, N.D.M.; Sidek, L.M.; Basri, H.; Hanapi, M.N.; Livia, L. Application of Integrated Flood Analysis System (IFAS) for Dungun River Basin. *IOP Conf. Ser. Earth Environ. Sci.* **2013**, *16*, 012128. [[CrossRef](#)]
43. Chen, Y.-C.; Gao, J.-J.; Bin, Z.-H.; Qian, J.-Z.; Pei, R.-L.; Zhu, H. Application study of IFAS and LSTM models on runoff simulation and flood prediction in the Tokachi River basin. *J. Hydroinformatics* **2021**, *23*, 1098–1111. [[CrossRef](#)]
44. Kimmany, B.; Ruangrassamee, P.; Visessri, S. Optimal Multi-Reservoir Operation for Hydropower Production in the Nam Ngum River Basin. *Eng. J.* **2020**, *24*, 1–13. [[CrossRef](#)]
45. Shahzad, A.; Gabriel, H.F.; Haider, S.; Mubeen, A.; Siddiqui, M.J. Development of a flood forecasting system using IFAS: A case study of scarcely gauged Jhelum and Chenab river basins. *Arab. J. Geosci.* **2018**, *11*, 383. [[CrossRef](#)]
46. Asghar, M.R.; Ushiyama, T.; Riaz, M.; Miyamoto, M. Flood and Inundation Forecasting in the Sparsely Gauged Transboundary Chenab River Basin Using Satellite Rain and Coupling Meteorological and Hydrological Models. *J. Hydrometeorol.* **2019**, *20*, 2315–2330. [[CrossRef](#)]
47. Ali, S.; Cheema, M.; Waqas, M.; Waseem, M.; Leta, M.; Qamar, M.; Awan, U.; Bilal, M.; Rahman, M. Flood Mitigation in the Transboundary Chenab River Basin: A Basin-Wise Approach from Flood Forecasting to Management. *Remote Sens.* **2021**, *13*, 3916. [[CrossRef](#)]
48. Ahmed, E.; Al Janabi, F.; Zhang, J.; Yang, W.; Saddique, N.; Krebs, P. Hydrologic Assessment of TRMM and GPM-Based Precipitation Products in Transboundary River Catchment (Chenab River, Pakistan). *Water* **2020**, *12*, 1902. [[CrossRef](#)]
49. Ahmed, E.; Al Janabi, F.; Yang, W.; Ali, A.; Saddique, N.; Krebs, P. Comparison of flow simulations with sub-daily and daily GPM IMERG products over a transboundary Chenab River catchment. *J. Water Clim. Chang.* **2022**, *13*, 1204–1224. [[CrossRef](#)]
50. Wagner, S.; Fersch, B.; Yuan, F.; Yu, Z.; Kunstmann, H. Fully coupled atmospheric-hydrological modeling at regional and long-term scales: Development, application, and analysis of WRF-HMS. *Water Resour. Res.* **2016**, *52*, 3187–3211. [[CrossRef](#)]
51. Givati, A.; Lynn, B.; Liu, Y.; Rimmer, A. Using the WRF Model in an Operational Streamflow Forecast System for the Jordan River. *J. Appl. Meteorol. Climatol.* **2011**, *51*, 285–299. [[CrossRef](#)]
52. Li, J.; Chen, Y.; Wang, H.; Qin, J.; Li, J.; Chiao, S. Extending flood forecasting lead time in a large watershed by coupling WRF QPF with a distributed hydrological model. *Hydrol. Earth Syst. Sci.* **2017**, *21*, 1279–1294. [[CrossRef](#)]
53. Gu, Y.; Peng, D.; Deng, C.; Zhao, K.; Pang, B.; Zuo, D. Atmospheric-hydrological modeling for Beijing’s sub-center based on WRF and SWMM. *Urban Clim.* **2022**, *41*, 101066. [[CrossRef](#)]
54. Ali, S.; Kiani, R.S.; Reboita, M.S.; Dan, L.; Eum, H.; Cho, J.; Dairaku, K.; Khan, F.; Shreshta, M.L. Identifying hotspots cities vulnerable to climate change in Pakistan under CMIP5 climate projections. *Int. J. Climatol.* **2021**, *41*, 559–581. [[CrossRef](#)]
55. Federal Floods Commission Government of Pakistan. Annual Flood Report for the Year 2020. Available online: <https://ffc.gov.pk/wp-content/uploads/2021/04/2020-Annual-Report-of-Oo-CEA-CFFC.pdf> (accessed on 10 September 2022).
56. Riaz, M.; Aziz, A.; Hussain, S. Flood Forecasting of an Ungauged Trans-boundary Chenab River Basin Using Distributed Hydrological Model Integrated Flood Analysis System (IFAS). *Pak. J. Meteorol.* **2017**, *13*, 51–62.
57. Carsell, K.M.; Pingel, N.D.; Ford, D.T. Quantifying the Benefit of a Flood Warning System. *Nat. Hazards Rev.* **2004**, *5*, 131–140. [[CrossRef](#)]
58. Hossain, F.; Katiyar, N.; Hong, Y.; Wolf, A. The emerging role of satellite rainfall data in improving the hydro-political situation of flood monitoring in the under-developed regions of the world. *Nat. Hazards* **2007**, *43*, 199–210. [[CrossRef](#)]
59. Awan, S. Pakistan: Flood Management-River Chenab from Marala to Khanki. *World Meteorol. Organ. Glob. Water Partnersh.* **2003**, 1–4. Available online: https://www.floodmanagement.info/publications/casestudies/cs_pakistan_chenab_sum.pdf (accessed on 10 September 2022).
60. Singh, P.; Ramasastri, K.S.; Kumar, N. Topographical Influence on Precipitation Distribution in Different Ranges of Western Himalayas. *Hydrol. Res.* **1995**, *26*, 259–284. [[CrossRef](#)]
61. Singh, P.; Jain, S.K.; Kumar, N. Estimation of Snow and Glacier-Melt Contribution to the Chenab River, Western Himalaya. *Mt. Res. Dev.* **1997**, *17*, 49. [[CrossRef](#)]
62. Kubota, T.; Shige, S.; Hashizume, H.; Aonashi, K.; Takahashi, N.; Seto, S.; Hirose, M.; Takayabu, Y.N.; Ushio, T.; Nakagawa, K.; et al. Global Precipitation Map Using Satellite-Borne Microwave Radiometers by the GSMaP Project: Production and Validation. *IEEE Trans. Geosci. Remote Sens.* **2007**, *45*, 2259–2275. [[CrossRef](#)]
63. Powers, J.G.; Klemp, J.B.; Skamarock, W.C.; Davis, C.A.; Dudhia, J.; Gill, D.O.; Coen, J.L.; Gochis, D.J.; Ahmadov, R.; Peckham, S.E.; et al. The Weather Research and Forecasting Model: Overview, System Efforts, and Future Directions. *Bull. Am. Meteorol. Soc.* **2017**, *98*, 1717–1737. [[CrossRef](#)]

64. Ekström, M. Metrics to identify meaningful downscaling skill in WRF simulations of intense rainfall events. *Environ. Model. Softw.* **2016**, *79*, 267–284. [[CrossRef](#)]
65. Srinivas, C.V.; Hariprasad, D.; Bhaskar Rao, D.V.; Anjaneyulu, Y.; Baskaran, R.; Venkatraman, B. Simulation of the Indian summer monsoon regional climate using advanced research WRF model. *Int. J. Climatol.* **2013**, *33*, 1195–1210. [[CrossRef](#)]
66. Patil, R.; Pradeep Kumar, P. WRF model sensitivity for simulating intense western disturbances over North West India. *Model. Earth Syst. Environ.* **2016**, *2*, 82. [[CrossRef](#)]
67. Lin, Y.-L.; Farley, R.D.; Orville, H.D. Bulk Parameterization of the Snow Field in a Cloud Model. *J. Clim. Appl. Meteorol.* **1983**, *22*, 1065–1092. [[CrossRef](#)]
68. Mlawer, E.J.; Taubman, S.J.; Brown, P.D.; Iacono, M.J.; Clough, S.A. Radiative transfer for inhomogeneous atmospheres: RRTM, a validated correlated-k model for the longwave. *J. Geophys. Res. Atmos.* **1997**, *102*, 16663–16682. [[CrossRef](#)]
69. Dudhia, J. Numerical Study of Convection Observed during the Winter Monsoon Experiment Using a Mesoscale Two-Dimensional Model. *J. Atmos. Sci.* **1989**, *46*, 3077–3107. [[CrossRef](#)]
70. Chen, F.; Dudhia, J. Coupling an Advanced Land Surface–Hydrology Model with the Penn State–NCAR MM5 Modeling System. Part I: Model Implementation and Sensitivity. *Mon. Weather Rev.* **2001**, *129*, 569–585. [[CrossRef](#)]
71. Hong, S.-Y.; Noh, Y.; Dudhia, J. A New Vertical Diffusion Package with an Explicit Treatment of Entrainment Processes. *Mon. Weather Rev.* **2006**, *134*, 2318–2341. [[CrossRef](#)]
72. Kain, J.S. The Kain–Fritsch Convective Parameterization: An Update. *J. Appl. Meteorol.* **2004**, *43*, 170–181. [[CrossRef](#)]
73. Hafiz, I.; Sidek, L.M.; Basri, H.; Fukami, K.; Hanapi, M.N.; Livia, L.; Jaafar, A.S. Integrated flood analysis system (IFAS) for Kelantan river basin. In Proceedings of the 2014 IEEE 2nd International Symposium on Telecommunication Technologies (ISTT), Langkawi, Malaysia, 24–26 November 2014; IEEE: Manhattan, NY, USA, 2014; pp. 159–162.
74. Chow, M.F.; Jamil, M.M. Review of development and applications of Integrated Flood Analysis System (IFAS) for flood forecasting in insufficiently-gauged catchments. *J. Eng. Appl. Sci.* **2017**, *12*, 9210–9215.
75. ICHARM/PWRI IFAS ver.2.0 Technical Manual. 2014, p. 40. Available online: https://www.pwri.go.jp/icharm/research/ifas/download_files/ifas_calibrator_ver_2_0_user_manual_e.pdf (accessed on 10 August 2022).
76. Nash, J.E.; Sutcliffe, J.V. River flow forecasting through conceptual models part I—A discussion of principles. *J. Hydrol.* **1970**, *10*, 282–290. [[CrossRef](#)]
77. Yapo, P.O.; Gupta, H.V.; Sorooshian, S. Automatic calibration of conceptual rainfall-runoff models: Sensitivity to calibration data. *J. Hydrol.* **1996**, *181*, 23–48. [[CrossRef](#)]
78. Moriasi, D.N.; Arnold, J.G.; van Liew, M.W.; Bingner, R.L.; Harmel, R.D.; Veith, T.L. Model Evaluation Guidelines for Systematic Quantification of Accuracy in Watershed Simulations. *Trans. ASABE* **2007**, *50*, 885–900. [[CrossRef](#)]
79. Givati, A.; Gochis, D.; Rummler, T.; Kunstmann, H. Comparing One-Way and Two-Way Coupled Hydrometeorological Forecasting Systems for Flood Forecasting in the Mediterranean Region. *Hydrology* **2016**, *3*, 19. [[CrossRef](#)]
80. Harris, L.M.; Durran, D.R. An Idealized Comparison of One-Way and Two-Way Grid Nesting. *Mon. Weather Rev.* **2010**, *138*, 2174–2187. [[CrossRef](#)]

Disclaimer/Publisher’s Note: The statements, opinions and data contained in all publications are solely those of the individual author(s) and contributor(s) and not of MDPI and/or the editor(s). MDPI and/or the editor(s) disclaim responsibility for any injury to people or property resulting from any ideas, methods, instructions or products referred to in the content.